Tractor Propeller-Pylon Interaction, Part I: Characterization of Unsteady Pylon Loading

de Vries, Reynard; Sinnige, Tomas; della Corte, B.; Avallone, Francesco; Ragni, Daniele; Eitelberg, Georg; Veldhuis, Leo

DOI
10.2514/6.2017-1175

Publication date
2017

Document Version
Accepted author manuscript

Published in
55th AIAA Aerospace Sciences Meeting

Citation (APA)
de Vries, R., Sinnige, T., della Corte, B., Avallone, F., Ragni, D., Eitelberg, G., & Veldhuis, L. (2017). Tractor Propeller-Pylon Interaction, Part I: Characterization of Unsteady Pylon Loading. In *55th AIAA Aerospace Sciences Meeting: Grapevine, Texas* Article AIAA 2017-1175 American Institute of Aeronautics and Astronautics Inc. (AIAA). https://doi.org/10.2514/6.2017-1175

Important note
To cite this publication, please use the final published version (if applicable).
Please check the document version above.

Tractor Propeller–Pylon Interaction, Part I: Characterization of Unsteady Pylon Loading

R. de Vries*, T. Sinnige†

Delft University of Technology, Delft, 2629 HS, The Netherlands

B. Della Corte‡

University of Naples Federico II, Naples, 80138, Italy

F. Avallone§, D. Ragni¶, G. Eitelberg‖, and L. L. M. Veldhuis**

Delft University of Technology, Delft, 2629 HS, The Netherlands

The impingement of the propeller slipstream on a downstream surface acts as a source of structure-borne noise. The experimental study presented in this paper aims at localizing and quantifying the main sources of unsteady loading for a pylon-mounted tractor-propeller configuration. Balance measurements showed that the installation of the pylon had no significant influence on the steady-state propeller performance. Measurements of the surface-pressure fluctuations on the pylon using microphones indicated harmonic unsteady loading at integer multiples of the blade-passage frequency, caused by the periodic interaction with the propeller blade wakes and tip vortices. The average amplitude of the pressure fluctuations on the pylon surface decreased by 85% between high thrust conditions ($J = 0.6$) and the zero thrust condition ($J \approx 1.0$). The main source of unsteady loading was the impingement of the blade tip vortices, which modified the pylon loading along the entire chord. Only at low thrust settings the impingement of the blade wakes on the leading edge of the pylon became dominant. The amplitude of the integral unsteady pylon loading showed a more complicated dependence on advance ratio, mainly due to relative phase differences between the excitations at different locations on the surface of the pylon. Increasing the propeller–pylon spacing decreased the amplitude of the unsteady pylon loading, without appreciably modifying the distribution of the pressure fluctuations over the pylon. Results show that a reduction of unsteady pylon loading can most effectively be achieved by surface treatments at the tip-vortex impingement region or with a pylon design optimized for specific operating conditions of the propeller.

I. Introduction

The high propulsive efficiency of propeller propulsion systems comes at the cost of increased noise compared to turbofans, both in terms of far-field as well as cabin noise levels. Conventional tractor propellers predominantly radiate noise in the propeller plane.[1] For pusher configurations, on the other hand, the noise emissions are typically amplified due to wake-impingement effects, which increase the noise levels especially away from the propeller plane.[2] From these considerations it can be concluded that cabin noise can be reduced by placing the propeller at the aft of the fuselage, in a pylon-mounted tractor configuration, as illustrated in Fig. 1. An additional advantage of such a configuration is the clean layout of the wing.

---

*M. Sc. Student, Flight Performance and Propulsion Section, Fac. of Aerospace Eng., reynarddevries@gmail.com.

†Ph. D. Candidate, Flight Performance and Propulsion Section, Fac. of Aerospace Eng., T.Sinnige@tudelft.nl, AIAA member.

‡M. Sc. Student, Fac. of Aerospace Eng.

§Postdoctoral Researcher, Aeroacoustics Section, Fac. of Aerospace Eng., F.Avallone@tudelft.nl, AIAA member.

¶Assistant Professor, Aeroacoustics Section, Fac. of Aerospace Eng., D.Ragni@tudelft.nl, AIAA member.

‖Full Professor, Flight Performance and Propulsion Section, Fac. of Aerospace Eng., AIAA member.

**Full Professor, Head of Flight Performance and Propulsion Section, Fac. of Aerospace Eng., AIAA member.

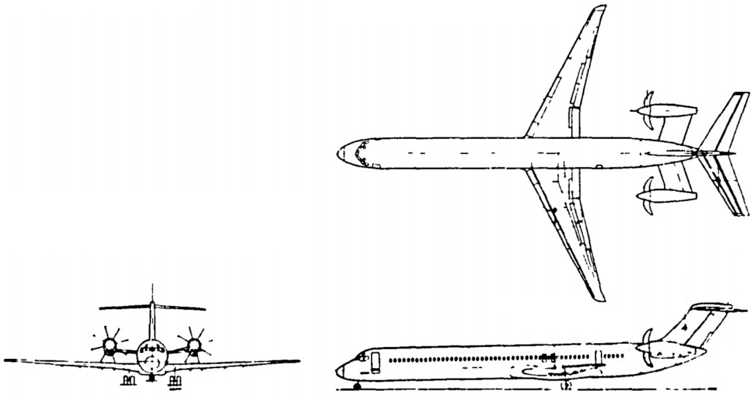

Figure 1. Aft-fuselage pylon-mounted tractor propeller concept, adapted from Ref. 3.

In a pylon-mounted tractor-propeller setup, the pylon is partially immersed in the propeller slipstream, similarly to a wing in conventional wing-mounted configurations. The resulting interaction effects can be separated into *downstream* and *upstream* effects.[4] The propeller slipstream changes the loading distribution on the downstream wing. The wing, on the other hand, perturbs the flowfield experienced by the upstream propeller, affecting its performance. In terms of noise generation, the same distinction can be made. Due to the upstream effect of the wing, the propeller blades operate under varying inflow conditions, presenting an additional noise source due to unsteady blade loading.[1] Meanwhile, the propeller slipstream induces fluctuating loads on the downstream wing, causing an additional source of noise. In addition to this airborne noise component, the associated structural vibrations lead to *structure-borne* noise, transmitted to the passengers via the excitation of the airframe.[5–7]

Structure-borne noise was extensively studied throughout the eighties.[5–14] It was shown that the propeller tip vortices are the main contributors to structure-borne noise.[5,10] The relevance of the structure-borne noise component was confirmed in the studies of Eversman et al.[12] and Miller et al.[8] The latter showed that the hydrodynamic pressure fluctuations on the wing surface induced by the tip vortex exceeded the pressure fluctuations on the fuselage caused by the direct airborne noise of the propeller by 20 dB (expressed as a sound pressure level). Moreover, Cole III et al.[9] found that, at the fuselage, the structure-borne sound due to unsteady wing loads was 15 dB higher than the airborne sound generated by the associated pressure fluctuations on the wing. This indicates that the interaction between the slipstream and the wing can be an important source of cabin noise without being a dominant source of radiated airborne noise.

The relative importance of structure-borne noise motivates studies of the unsteady loads acting on a wing or pylon immersed in a propeller slipstream. Characteristics of the aerodynamic excitation of a wing caused by propeller-slipstream impingement have been discussed before in both analytical[7,15] and experimental[10,16–18] investigations. However, these studies are limited in several aspects. Firstly, no detailed information is presented regarding the time-dependent spatial distribution of pressure over the wing. Secondly, the integrated effect of the unsteady pressure distribution on overall unsteady wing loading is not quantified. Consequently, there is no systematic study of the effect of key parameters such as advance ratio or angle of attack on overall unsteady wing or pylon loading.

The study discussed in the present paper quantifies the unsteady aerodynamic loading on a pylon immersed in the slipstream of a tractor propeller. For this purpose, the evolution of the slipstream surrounding the pylon and consequent pressure fluctuations on the pylon surface are analyzed. A discussion is held on how these unsteady pressure distributions can be integrated in order to obtain scalar parameters which allow evaluating the overall unsteady pylon loading for different operating conditions from a structure-borne noise point of view.

II. Experimental Setup

II.A. Wind-Tunnel Facility and Models

The experimental campaign was carried out in the low-speed Low-Turbulence Tunnel (LTT) at Delft University of Technology. The LTT is a closed test section, closed-circuit wind tunnel, with a maximum wind velocity of 120 m/s. The inflow turbulence level equals 0.02% for freestream velocities between $U_\infty = 10$ m/s and $U_\infty = 40$ m/s. The test section has a cross-section of 1.8 m x 1.25 m.

A pylon-mounted tractor-propeller configuration was simulated by positioning a propeller model at the tip of a symmetric wing, as depicted in Fig. 2. The four-bladed propeller model featured a diameter of $D = 0.236$ m and maximum blade chord of 17.9 mm, with a blade pitch angle of 23° at 75% of the radius. Additional details of the propeller geometry are provided in Ref. 19. The pylon model featured a NACA 0012 cross-section and a straight, untapered planform with a chord of $c = 0.200$ m and span of $b = 0.592$ m.

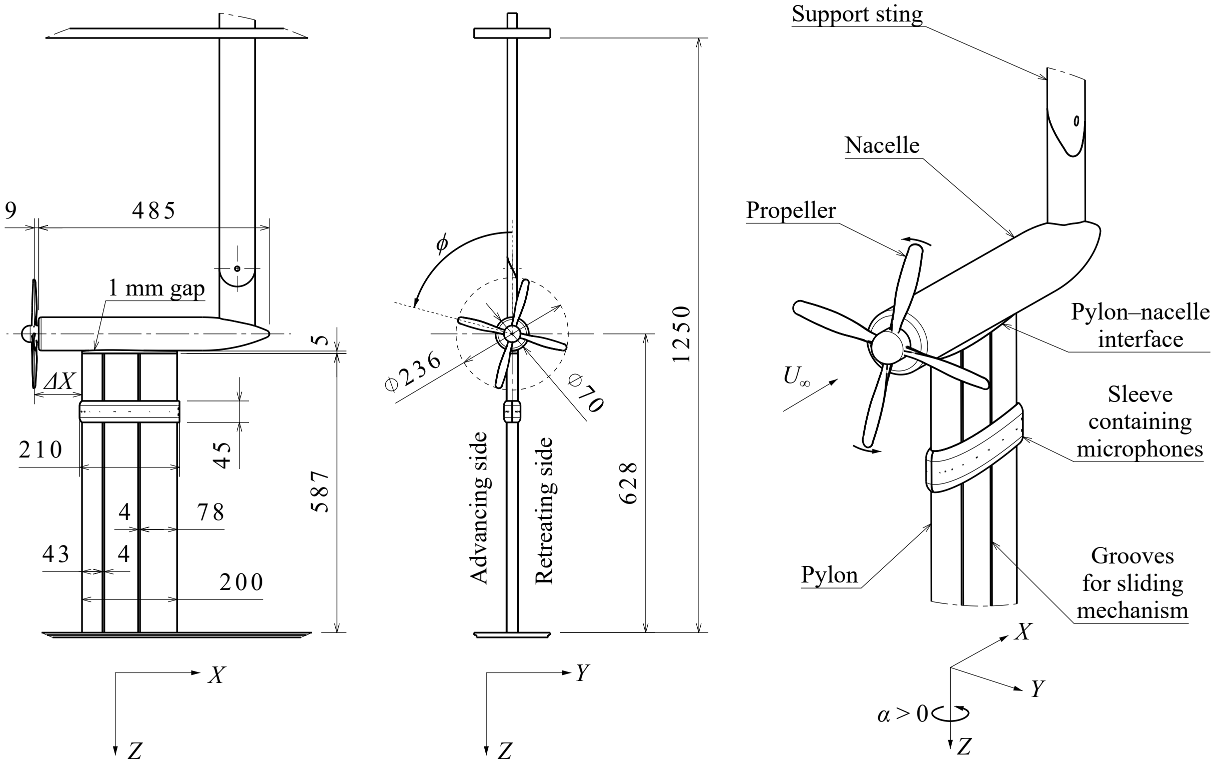

Figure 2. Schematic representation of the experimental model and its components. All dimensions are in mm.

The propeller and nacelle were connected to a six-component external balance via a vertical support sting, while the pylon was mounted directly to the floor of the wind tunnel. A 1 mm gap was left between the pylon–nacelle interface and the nacelle to allow for measurements of the propeller thrust using the external balance. The axial position of the pylon could be changed to vary the distance between propeller plane and pylon leading edge. A range of propeller–pylon spacings of $0.21 \leq \Delta X/D \leq 0.85$ was selected based on typical aircraft layouts, with the intermediate value of $\Delta X/D = 0.42$ selected as baseline value. The entire setup could be rotated around the Z-axis to allow measurements at angle of attack, defined positive for an inboard-up rotating propeller, as indicated in Fig. 2.

II.B. Measurement Techniques

The characteristics of the propeller slipstream define the unsteady pylon loading. Therefore, the propeller performance was acquired using an external balance and particle-image velocimetry (PIV) was employed to measure the velocity and pressure fields in the propeller slipstream. The unsteady pylon loading was subsequently quantified using surface microphones. Although additional measurement techniques were employed as well, only the ones relevant for the subset of measurement results included in this paper are presented.

II.B.1. External Balance

The propeller thrust was acquired during the entire test campaign by connecting the propeller and nacelle to an external six-component balance. Since the pylon was not physically connected to the nacelle, the balance only measured loads on the propeller, nacelle, and support sting. The net propeller thrust was calculated by subtracting the propeller-off thrust, i.e. the thrust measured at the same freestream conditions but with the propeller removed and replaced by a dummy hub: $T_{\text{net}} = T - T_{\text{off}}$. The net thrust therefore includes a minor interference drag contribution due to the variations in velocity created over the nacelle and support sting by the propeller slipstream. The propeller thrust coefficient was then calculated as:

$$C_T = \frac{T_{\text{net}}}{\rho_\infty n^2 D^4}, \tag{1}$$

where ρ_∞ is the density of the freestream and n the rotational velocity of the propeller in revolutions per second. The thrust coefficient presented a measurement uncertainty of 0.3% at the baseline advance ratio of $J = U_\infty/(nD) = 0.8$. Furthermore, to verify the repeatability of the experiment, a subset of measurements was repeated after several days and configuration changes, registering a 2% variation in thrust coefficient.

II.B.2. Surface Microphones

The pressure fluctuations on the pylon were measured using a sleeve containing sixteen microphones, which could be traversed in the spanwise direction of the pylon through two grooves on each side of the pylon. Eight Sonion 8010T microphones were installed along the midline on each side of the sleeve, with a higher chordwise spacing density near the leading edge for a locally increased resolution of the impingement phenomena, as indicated in Fig. 3. The microphones measured in a frequency range of 10 Hz–11.5 kHz, with a maximum input level of 112 dB (re 20×10^{-6} Pa) at 1 kHz and an equivalent noise level of 28 dBA. A frequency-dependent calibration was carried out using a LinearX M53 reference microphone, which was calibrated by means of a GRAS 42AA piston phone. The resonance frequency of the cavity was found to be 16.8 kHz, which was sufficiently high to not affect the measurements of the slipstream-impingement phenomena.

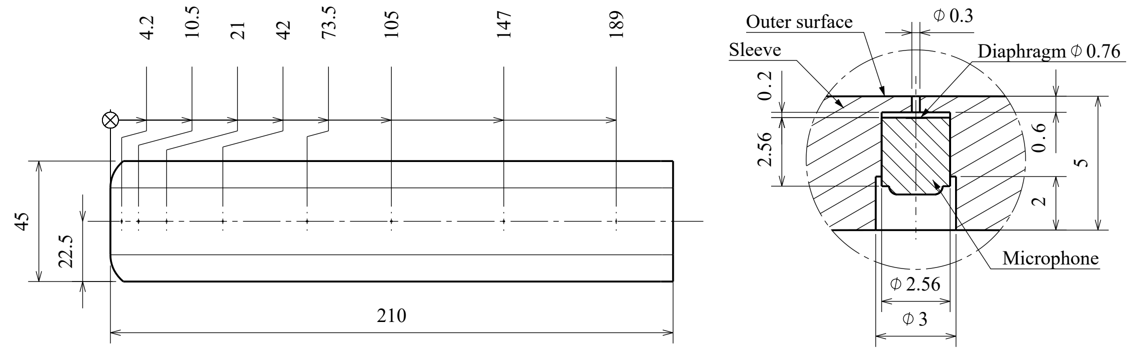

Figure 3. Sleeve dimensions, indicating microphone locations (left), and close-up of the microphone installation (right). All dimensions are in mm.

A 5 mm sleeve thickness was required in order to house the microphones. Consequently, the outer profile of the sleeve was shaped by taking a 5 mm offset with respect to the NACA 0012 cross-section of the clean pylon model, in the direction normal to the local curvature. Approximately seventy spanwise positions were measured, with variable spacing ranging from 1 mm near the propeller blade-tip region to 5 mm far outside the propeller slipstream. The acquisition time for each measurement was 30 seconds, at a sampling rate of 25.6 kHz. For a typical operating condition considered ($U_\infty = 10$ m/s, $J = 0.8$) this implies approximately 1600 complete revolutions with 480 samples per revolution.

The pressure spectra obtained in the propeller wake region were dominated by tonal components, which clearly stood out of the broadband noise. These strong tonal components were not visible outboard of the propeller slipstream, indicating that the recorded pressure fluctuations were of hydrodynamic origin, and not due to radiated noise of the propeller. A number of measurements were carried out multiple times to verify the repeatability of the surface-microphone measurements. On average, the rms of the pressure waveforms showed a 5% variation between measurements repeated after several days and setup modifications. This value is indicative of the uncertainty associated with the surface-pressure measurements.

II.B.3. Particle-Image Velocimetry

Two different PIV setups were used, as illustrated in Fig. 4. The isolated propeller slipstream was evaluated with a stereoscopic PIV setup. The tip-vortex impingement process on the pylon, on the other hand, was measured using a high-resolution planar PIV setup in the vicinity of the pylon leading edge. For the propeller-slipstream plane, pressure fields were computed from the velocity fields by numerically integrating the incompressible Navier–Stokes equations following a finite-difference approach.[20] For this purpose, the Poisson solver outlined in Ref. 19 was used. PIV uncertainty analysis was carried out following the procedure of Refs. 21 and 22, assuming linear error propagation and independent variables.

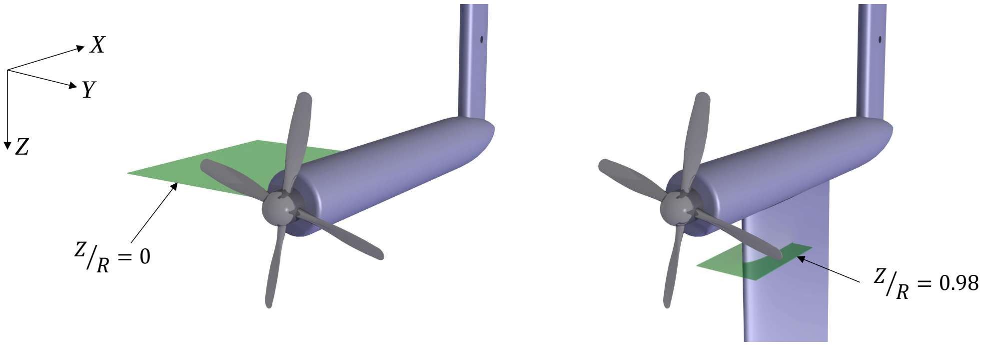

Figure 4. PIV planes analyzed: isolated propeller slipstream (left) and pylon leading edge (right).

A SAFEX Twin Fog DP generator with SAFEX Inside Nebelfluid was used for flow seeding. The mixture of diethylene-glycol and water generates tracer particles with an average diameter and relaxation time of the order of 1 μm and 1 μs respectively. A 200 mJ Quantel Evergreen laser provided illumination for the propeller-slipstream setup. For the pylon leading-edge setup, where both sides of the pylon had to be illuminated simultaneously, also a 200 mJ Quantel Twin BSL laser was used. Two LaVision Imager Pro LX CCD cameras (12 bit) were employed with Nikkor 200 mm f/4 lenses for image acquisition, at a rate of 0.78 Hz. The cameras feature a 4872 × 3248 pixel sensor, with a pixel size of 7.4 μm. Image processing was carried out using LaVision Davis 8.3 software. For all phase-locked measurements 300 images were acquired per selected phase angle, while for uncorrelated measurements 500 images were recorded. The main characteristics of the two PIV setups are provided in Table 1.

Table 1. Main parameters of the two PIV setups. Velocity and pressure uncertainties are expressed as a percentage of freestream velocity and freestream dynamic pressure respectively.

PIV setup:	**Slipstream (Stereoscopic)**	**Leading Edge (Planar)**
Focal length [mm]	200	200
Magnification	0.164	0.371
Field of view [mm^2]	230 × 210	60 × 180
Imaging resolution [pixel/mm]	18	50
Window size [pixel^2]	12 × 12	24 × 24
Overlap factor [%]	75	50
Spatial resolution [mm]	0.7	0.5
Spatial dynamic range	79	31
Velocity uncertainty [%]	1.6	1.2
PIV pressure uncertainty [%]	2.9	–

II.C. Test Conditions

The majority of the test campaign was performed at a freestream velocity of 10 m/s, which was selected to optimize the dynamic range of the microphone measurements. This corresponds to a Reynolds number based on the pylon chord of $Re_c = 1.37 \cdot 10^5$. In addition, PIV measurements were taken at 40 m/s, since in the companion study[23] higher freestream velocities were required. Three parameters were varied during the experiments: advance ratio, angle of attack, and propeller–pylon spacing. The first two were considered of interest since these parameters vary during aircraft operation. Given that for all surface-pressure measurements the freestream velocity and blade pitch angle were kept constant, the advance ratio is indicative of propeller thrust and is directly tied to the slipstream structure. Propeller–pylon spacing, on the other hand, was analyzed since it is a relatively unconstrained parameter during the design process, and was shown to have an effect on the structure-borne noise levels in earlier studies.[5] The considered ranges of advance ratio and angle of attack were based on previous experience with the propeller model and selected such that blade and pylon stall were avoided. The baseline advance ratio was selected to be $J = 0.8$, since preliminary results showed that this value represented a moderate thrust setting. The baseline angle of attack was set to $\alpha = 0°$ for simplicity. The operating conditions are summarized in Table 2. At each operating point, measurements were taken both with the propeller on and with the propeller removed. The results presented in this paper are given for the baseline configuration, unless explicitly mentioned otherwise.

Table 2. Overview of the test conditions.

Variables	Values	Baseline value
Freestream velocity U_∞ [m/s]	[10, 40]	10
Advance ratio J	[0.7, 0.8, 0.9, 1.0]	0.8
Angle of attack α [deg]	[–6, 0, +6, +12]	0
Propeller–pylon spacing $\Delta X/D$	[0.21, 0.32, 0.42, 0.53, 0.64, 0.85]	0.42

III. Structure-Borne Noise Indicators

III.A. Definition of Variables

To quantify in-cabin structure-borne noise levels, detailed knowledge of both the structural characteristics of the airframe and the aerodynamic forcing is required. In the case of air–structure interactions, it is possible to study the aerodynamic excitation separately without considering the feedback from the structural vibrations into the surrounding medium.[14] For this purpose, it is necessary to define a parameter which allows comparing the expected structure-borne noise levels in different operating conditions, independently of the characteristics of the actual structure. For the definition of this parameter, it is of interest to distinguish two extreme cases of structural properties. The first is a situation where all vibrational energy is transmitted into the structure. This means that the displacement of the structure is in-phase with the excitation at each location, implying a freely deformable structure (i.e. continuity between adjacent elements of the structure may not be maintained). In this case, integrating the amplitude of the pressure fluctuations over the pylon is representative of the expected structure-borne noise levels. For this reason $\tilde{C}_{p,\mathrm{mean}}$ is defined, which indicates the average over the pylon surface of the rms of the pressure fluctuations at each location, i.e.:

$$\tilde{C}_{p,\mathrm{mean}} = \frac{1}{2c(r_{\max} - r_{\min})q_\infty} \int_{r_{\min}}^{r_{\max}} \int_0^c \left(\sqrt{\frac{1}{2\pi} \int_0^{2\pi} \tilde{p}^2_{\mathrm{adv}}\,(x, r, \phi)\,\mathrm{d}\phi} + \sqrt{\frac{1}{2\pi} \int_0^{2\pi} \tilde{p}^2_{\mathrm{retr}}\,(x, r, \phi)\,\mathrm{d}\phi} \right) \mathrm{d}x\mathrm{d}r, \tag{2}$$

where $r_{\min}$ and $r_{\max}$ refer to the lower and upper limits of the spanwise interval evaluated, q_∞ is the freestream dynamic pressure, ϕ is the propeller phase angle, and x and r are the axial and radial coordinates over the pylon, respectively. The pressure-fluctuation amplitude $\tilde{p}$ on the advancing and retreating blade sides has been separated into two terms since the same x coordinate is shared, but essentially the mean is taken over the entire pylon surface.

However, since in the case of $\tilde{C}_{p,\mathrm{mean}}$ all phase-related information has been removed by taking the rms before integrating over the surface, two pylons with different net loading functions can have the same $\tilde{C}_{p,\mathrm{mean}}$ value. Therefore, it is of interest to consider a second case, which is a perfectly rigid pylon structure, i.e. Young's modulus $E \to \infty$, implying infinite wave propagation speed in the medium. For this case all loads are instantaneously transmitted throughout the pylon. Under this assumption, a total aerodynamic forcing function $\tilde{C}_L(\phi)$ obtained by integrating the loads on the surface for each instant of time will be representative of the structure-borne noise levels. The rms of this function, $\tilde{C}_{L,\mathrm{rms}}$, is therefore a scalar parameter which allows comparing the overall unsteady pylon loading in different operating conditions, given by:

$$\tilde{C}_{L,\mathrm{rms}} = \frac{1}{(r_{\max} - r_{\min})cq_\infty} \sqrt{\frac{1}{2\pi} \int_0^{2\pi} \left(\int_{r_{\min}}^{r_{\max}} \int_0^c \Delta\tilde{p}\,(x, r, \phi)\,\mathrm{d}x\mathrm{d}r \right)^2 \mathrm{d}\phi}, \tag{3}$$

where $\Delta\tilde{p} = (\tilde{p}_{\mathrm{retr}} - \tilde{p}_{\mathrm{adv}})$ is the difference between the pressure-fluctuation amplitude on each side of the pylon.

However, in real structures the wave propagation speed is finite and depends on the type of wave.[24] Structural waves can be longitudinal, transverse (shear and torsion), or flexural (i.e. bending). Typically, it can be considered that the loads are instantaneously transmitted throughout the structure if the associated structural wavelength is more than six times the characteristic length of the area over which loads are applied. In such case, the load distribution can be substituted by a point load.[25] Preliminary estimations of the structural wavelengths for a typical pylon-mounted propeller configuration show that, for longitudinal and transverse waves, the pylon can be considered rigid from this point of view. However, for flexural waves the structural wavelength is typically larger than the pylon but not large enough to consider the pylon perfectly rigid. Therefore, $\tilde{C}_{L,\mathrm{rms}}$ is more representative of structure-borne noise levels for a typical aircraft configuration than $\tilde{C}_{p,\mathrm{mean}}$, but none of the two will have a strictly bijective relation with the perceived noise levels in the cabin. Nonetheless, even if the structural wavelength is not substantially longer than the size of the affected area, integrating the pressure distribution to obtain a lift coefficient will still provide a preliminary estimate of the total unsteady loading transmitted through the structure.

III.B. Unsteady Pressure Coefficient

The recorded microphone data were processed to exclude non-harmonic signals that were unrelated to the periodic impingement of the propeller slipstream. To this end, the recorded pressure signal was divided into individual rotations using a one-per-revolution trigger signal, and averaged per phase angle over all rotations (*phase-averaging*). It was verified that the acquisition time was sufficient for the phase-averaging process to converge. Using the phase-averaged waveform obtained at each measurement location, $\tilde{C}_{p,\mathrm{mean}}$ can be calculated with Eq. 2. All pressures and loads presented in the following sections are based on the phase-averaged waveforms, expressed as an unsteady pressure coefficient $\tilde{C}_p(\phi) = \tilde{p}(\phi)/q_\infty$.

III.C. Unsteady Lift Coefficient

For an accurate estimate of the rms of the unsteady lift coefficient ($\tilde{C}_{L,\mathrm{rms}}$), the spatial and temporal spacing between consecutive sampling points must be smaller than the characteristic wavelength and period of the excitation, respectively. While high temporal and radial resolutions were available, the axial separation between microphones ranged from 6.3 mm near the leading edge to 42 mm near the trailing edge (see Fig. 3). On the other hand, the distance between consecutive blade wakes for the baseline case was approximately $U/(n \cdot B) = 47$ mm (where B is the number of blades of the propeller). For this reason, the recorded pressure-fluctuation distributions were interpolated to a finer grid by carrying out a linear interpolation between each pair of consecutive microphones, decreasing the axial separation between subsequent points by a factor ten. This was sufficient to achieve convergence of the resulting unsteady lift coefficient. Radial velocities were neglected, since the microphone data indicated that on the pylon surface the radial velocity is small when compared to the axial velocity, as will be shown later. A schematic representation of the interpolation procedure between two consecutive microphones is depicted in Fig. 5.

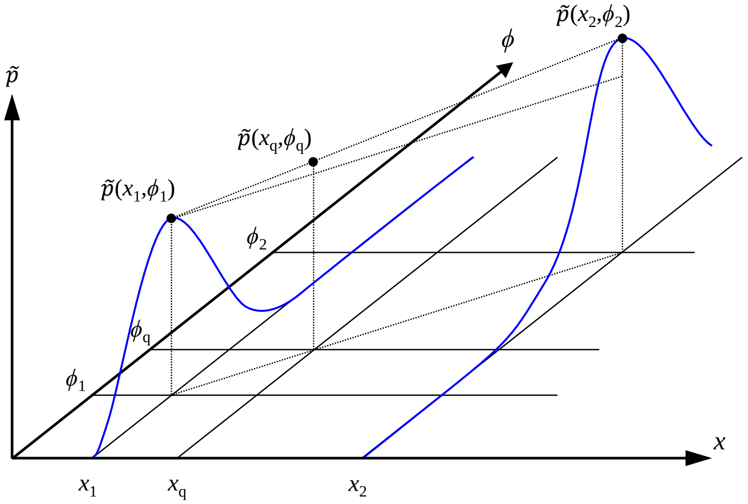

Figure 5. Graphical representation of the pressure interpolation procedure between two consecutive microphones located at x_1 and x_2.

For a generic query point x_q situated between x_1 and x_2, each phase angle $\phi_\mathrm{q} \in (0, 2\pi]$ was evaluated. However, as visible in Fig. 5, the pressure $\tilde{p}(x_\mathrm{q}, \phi_\mathrm{q})$ cannot be obtained from the pressures at the upstream and downstream microphones at the same phase angle ϕ_q. Instead, the pressure $\tilde{p}(x_\mathrm{q}, \phi_\mathrm{q})$ corresponds to a flow structure which was at x_1 at a past time instant ϕ_1 and will arrive at x_2 at a future time instant ϕ_2. Furthermore, during this displacement the pressure amplitude of the flow structure may vary due to e.g. dissipation. Supposing constant convective velocity in the axial segment and a linear pressure evolution for simplicity, from Fig. 5 it is evident that:

$$\frac{\tilde{p}(x_\mathrm{q}, \phi_\mathrm{q}) - \tilde{p}(x_1, \phi_1)}{\tilde{p}(x_2, \phi_2) - \tilde{p}(x_1, \phi_1)} = \frac{\phi_\mathrm{q} - \phi_1}{\phi_2 - \phi_1} = \frac{x_\mathrm{q} - x_1}{x_2 - x_1}. \tag{4}$$

The pressure amplitude $\tilde{p}(x_\mathrm{q}, \phi_\mathrm{q})$ can be obtained from the equalities of Eq. 4 if ϕ_1, ϕ_2, or $\Delta\phi = \phi_2 - \phi_1$ is known. Therefore the problem is reduced to finding the phase difference $\Delta\phi$ or convective velocity V_conv corresponding to the axial segment between the two microphones, since the phase difference is related to the convective velocity of the microphone segment through:

$$\Delta\phi = \frac{2\pi n}{V_\mathrm{conv}}(x_2 - x_1). \tag{5}$$

In order to obtain the convective velocity, the procedure of Ref. 26 was followed, which consists of obtaining the phase angle φ of the cross spectral density (CSD) function of the two (raw) pressure signals. Note that the CSD phase angle φ is not equal to the propeller-blade phase angle ϕ. If φ is plotted versus frequency, a sawtooth-like function is obtained. The inverse of the slope of this function, $\partial f / \partial \varphi$, can then be related to the convective velocity V_conv through:

$$V_\mathrm{conv} = 2\pi(x_2 - x_1)\frac{\partial f}{\partial \varphi}. \tag{6}$$

IV. Results

IV.A. Propeller Performance

Before evaluating the unsteady loading on the pylon, the steady propeller thrust was measured. Figure 6 plots the thrust coefficient (see Eq. 1) generated by the propeller versus advance ratio, with the pylon installed (*installed propeller)* and removed (*isolated propeller*). The 2% variation on the balance data identified by analysis of repeated measurements at constant operating conditions is indicated by the errorbars.

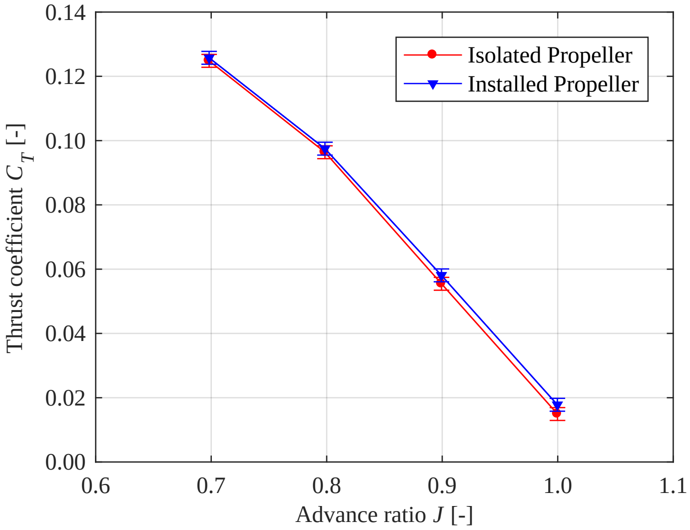

Figure 6. Isolated and installed propeller thrust coefficient versus advance ratio ($U_\infty = 40$ m/s).

Figure 6 displays the expected increase in blade loading with decreasing advance ratio. The response became non-linear at the highest thrust setting due to the onset of separation on the blades. Comparing the isolated and installed configurations, Fig. 6 suggests that installation of the pylon causes a minor increase in thrust coefficient (1.2% at the baseline $J = 0.8$). This variation was however within the repeatability of the measurement data. In any case, it can be confirmed that for the baseline propeller–pylon spacing value the upstream effect of the pylon on the integral propeller loading is small. Regarding the effect of the pylon on unsteady blade loading, no values can be obtained at this stage.

Stereoscopic PIV was used to measure the flowfield in the propeller slipstream. Figure 7a presents contours of the axial velocity difference with respect to the propeller-off case. The axial velocity difference $\Delta U = U - U_{\text{off}}$ is presented in order to clearly identify the effect of the blade wakes and tip vortices. Figure 7b displays the associated distribution of the static pressure coefficient $C_p = (p - p_\infty)/q_\infty$. Contour lines of constant normalized vorticity have been included in both plots to indicate the position of the blade wakes and vortices. Normalized vorticity is defined as $\omega^* = \omega D / U_{\text{eq}}$, with the equivalent velocity at the propeller disk U_{eq} used in order to include the effect of propeller loading in the nondimensionalization. The equivalent velocity at the propeller disk was estimated using simple actuator-disk theory (see e.g. Ref. 4).

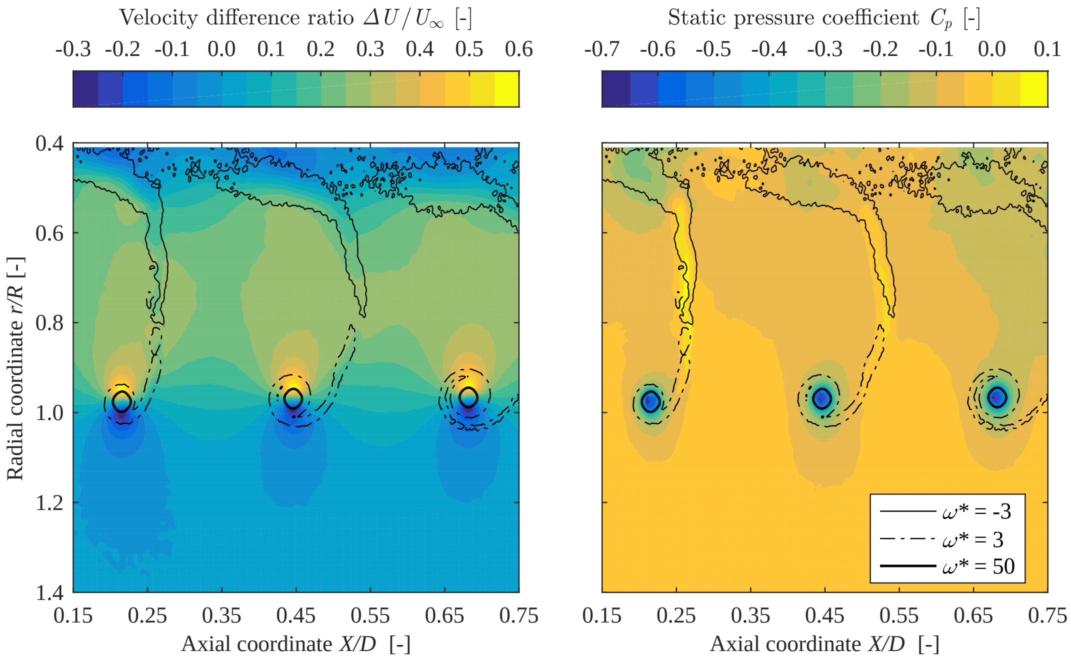

a) Velocity difference ratio

b) Static pressure coefficient

Figure 7. Axial velocity difference (left) and static pressure (right) distributions in the isolated propeller slipstream, with contours of constant normalized vorticity indicated ($U_\infty = 40$ m/s).

Figure 7a shows strong velocity perturbations induced locally by the tip vortices, while the root vortices were less concentrated. Pressure evaluation of the ensemble-averaged PIV fields (not included here) indicated that maximum blade loading occurred around 75% of the blade span. Thus, the vorticity in the blade wakes was mainly positive outboard of this radial station, and negative inboard, as visible in Fig. 7a. For the same reason, the radial segment around $r/R = 0.75$ presented the highest acceleration in the slipstream, and as a consequence the blade wakes—which were practically straight immediately behind the propeller disk—gradually became more crescent as they were convected downstream.

The tip vortices presented strong suction peaks due to the centrifugal forces in the vortex core, as shown in Fig. 7b. The root vortices, meanwhile, indicated only a slight decrease in pressure with respect to the surrounding flow. The blade wakes featured a low but positive pressure coefficient. This increased static pressure rapidly recovered to ambient pressure as the blade wakes were convected downstream. Finally, in the slipstream region between the blade wakes, the pressure coefficient was practically zero, though slightly higher behind the propeller disk than further downstream. The variations in velocity magnitude and direction and static pressure visible in Fig. 7 are the sources of unsteady loading on a pylon when it is immersed in the propeller slipstream.

IV.B. Slipstream-Induced Pressure Fluctuations on the Pylon

The data presented in the following paragraphs were obtained from the microphone measurements at the surface of the pylon sleeve. Figure 8 provides the unsteady pressure distribution over the pylon surface for the baseline configuration. In Fig. 8 the flow direction is from left to right and the black dots indicate the measurement locations, while red crosses mark the positions at which the associated pressure waveforms are plotted in Figs. 9 and 10. The unsteady pressure distribution is represented by means of the rms of the unsteady pressure coefficient using logarithmic scale, i.e. the unsteady pressure is expressed in dB taking freestream dynamic pressure as reference value.

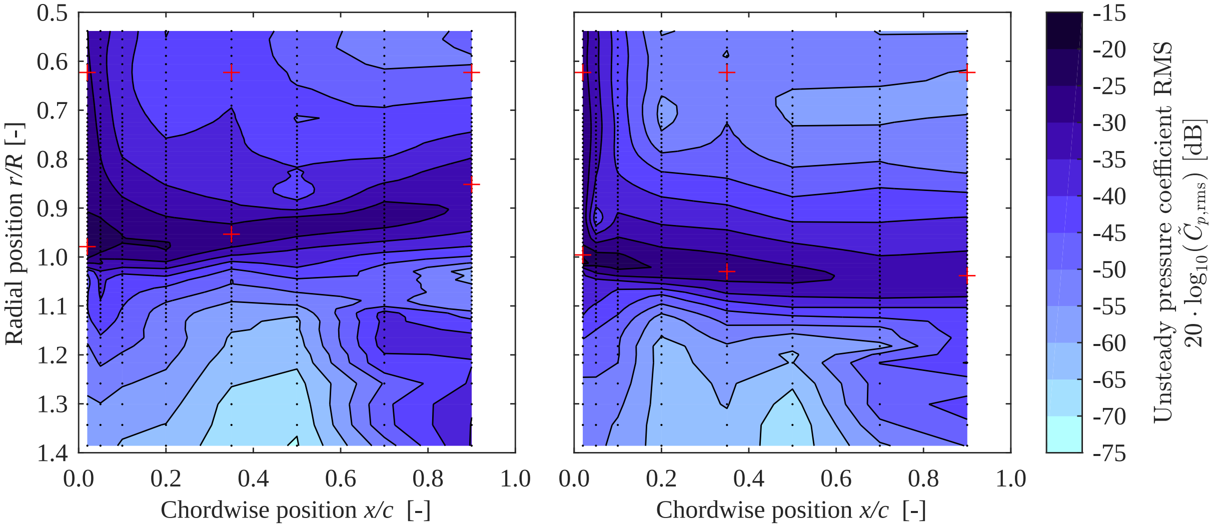

a) Retreating side **b) Advancing side**

Figure 8. Contours of the rms of the pressure fluctuations over the pylon surface in the baseline configuration, expressed in logarithmic scale relative to freestream dynamic pressure.

Figure 8 shows that in the baseline configuration the tip vortex was the dominant source of pressure fluctuations. These fluctuations displayed a maximum at the leading edge of the pylon, but persisted as the tip vortex was convected along the chord. Johnston and Sullivan[17] attributed the gradual decrease in amplitude of the pressure fluctuations along the chord to viscous interaction between the boundary layer and vortex core. The inflow perturbation due to the blade wakes, meanwhile, mostly affected the leading edge of the pylon. The blade wakes were characterized by reduced axial velocity and increased tangential velocity, hence affecting the angle of attack perceived by the pylon. At high advance ratios, when blade loading—and, therewith, tip vortex strength—tended to zero, the blade wakes remained and became the dominant source of pressure fluctuations. In the freestream region ($r/R_\mathrm{p} > 1$), the pressure fluctuations were lowest, although they increased towards the trailing edge due to boundary-layer transition.

A spanwise displacement of the tip vortex is clearly visible in Fig. 8. This displacement has been described in earlier studies[4, 15, 17] and is attributed to the variations in lift along the pylon span. In the propeller slipstream, the induced angle of attack and increased dynamic pressure cause the pylon to generate lift, while outboard of the slipstream the lift tends to zero (under the symmetric inflow conditions considered). The spanwise variations in circulation induce an inboard-oriented velocity on the retreating blade side and an outboard-oriented velocity on the advancing blade side, where the swirl velocity component of the slipstream stagnates on the pylon surface. As a consequence, the tip vortex gradually displaces inboard on the retreating side and outboard on the advancing side.

Additional contour maps of the pressure fluctuations for different operating conditions, omitted here, showed an increased spanwise displacement of the tip vortex with decreasing advance ratio. This was due to the associated increase in swirl angle and dynamic pressure of the slipstream. At negative angles of attack, the spanwise displacement increased due to the gradual alignment of the slipstream with the freestream velocity direction, while for positive angles of attack the spanwise displacement was reduced. At $\alpha = +6°$, the spanwise displacement had practically disappeared and a separation bubble appeared on the retreating (suction) side of the pylon. In this case the reattachment of the flow behind the separation bubble became the dominant source of pressure fluctuations on the retreating side, rather than the tip vortex. At $\alpha = +12°$, the flow on the retreating side was fully separated. Varying the propeller–pylon spacing showed no significant effect on the unsteady pressure distribution on the pylon, while the levels gradually decreased with increasing spacing because of dissipation.

The pressure fluctuations on the pylon surface can be visualized by plotting the unsteady pressure waveform versus phase angle, as depicted in Figs. 9 and 10. Figure 9 illustrates the waveforms in the blade-wake region ($r/R = 0.62$), while Fig. 10 shows the waveforms along the path of the tip vortex ($r/R \approx 1$). In both figures three axial locations are presented: a measurement location near the leading edge ($x/c = 0.02$), near the trailing edge ($x/c = 0.90$), and one intermediate location ($x/c = 0.35$). The small variations in amplitude between consecutive peaks of the waveforms in Figs. 9 and 10 are caused by components of the signal that are integral multiples of the propeller rotational speed, but non-integer multiples of the blade-passage frequency. These components remained after the phase-averaging process, but are irrelevant compared to the dominant tonal response at the blade-passage frequency.

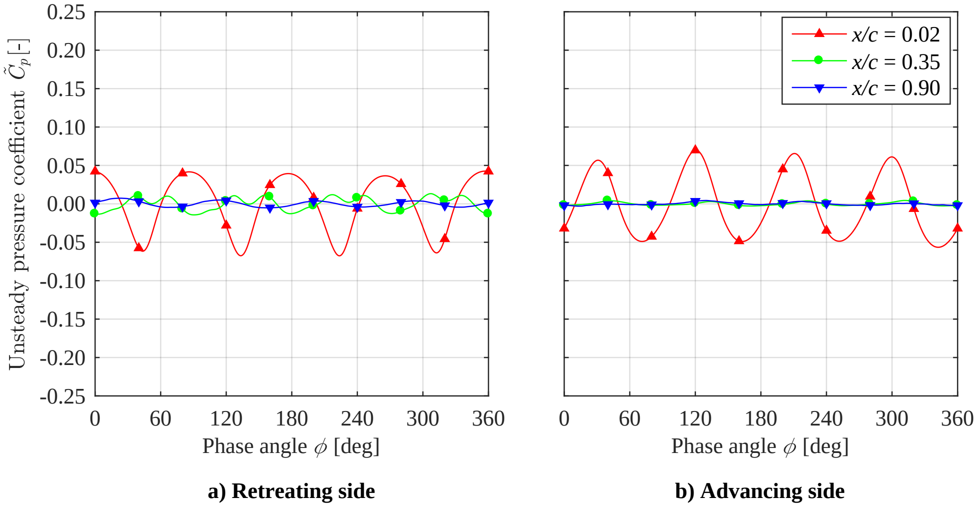

Figure 9. Pressure fluctuations at three chordwise locations in the blade-wake region ($r/R = 0.62$) for the baseline configuration.

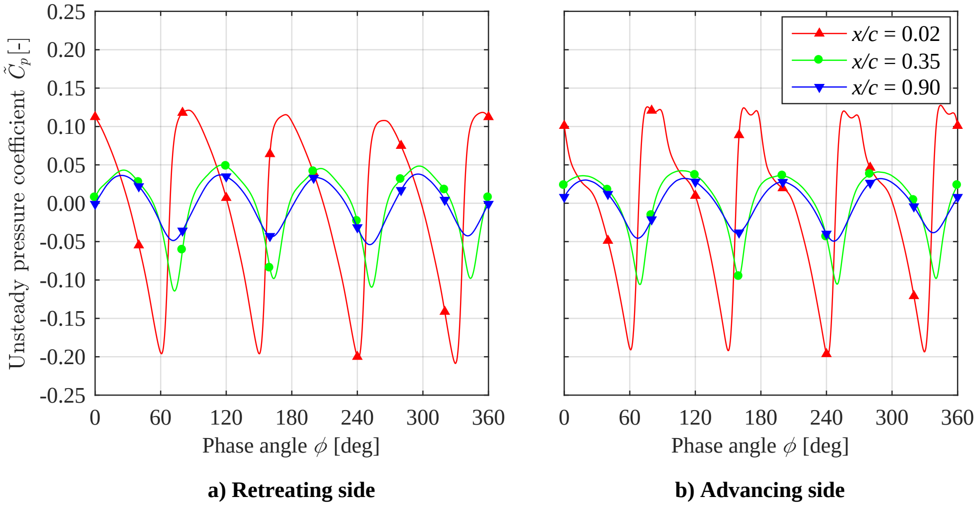

Figure 10. Pressure fluctuations at three chordwise locations along the path of the tip vortex for the baseline configuration. The chordwise locations $x/c = (0.02, 0.35, 0.90)$ correspond to radial locations $r/R = (0.98, 0.95, 0.85)$ on the retreating side and $r/R = (1.00, 1.03, 1.04)$ on the advancing side, respectively.

Figure 9 shows that in the blade-wake region the pressure waveform is quasi-sinusoidal at the leading edge, and then rapidly diminishes in amplitude downstream along the chord. In the tip-vortex region (Fig. 10), meanwhile, sharp negative peaks are visible in the waveforms at the leading edge ($x/c = 0.02$), created by the low pressure in the vortex core. These pronounced peaks were composed of multiple harmonics, and thus at the leading edge the pressure spectra presented strong tonal components for numerous multiples of the blade-passage frequency. It should be highlighted that pressure *fluctuations* are presented, i.e. the value $\tilde{C}_p = 0$ does not correspond to the actual static pressure value in the propeller slipstream between wake/tip-vortex passages. As the vortex moves downstream the peaks become less sharp, until finally toward the trailing edge again a quasi-sinusoidal waveform is obtained. This gradual decrease in amplitude of the fluctuations was attributed to viscous interaction between the boundary layer and the vortex core, as discussed before in relation to Fig. 8.

At the leading edge in the tip-vortex impingement region, the amplitude of the pressure fluctuations was similar on both sides of the pylon. However, the waveforms on the two sides of the pylon differed in shape. Two main factors can be identified as the cause of the differences between the pressure distributions on the two sides of the pylon. Firstly, while the vortex core causes a suction peak on both sides of the pylon, the effect of the blade wakes (which roll up into the vortex) on the perceived angle of attack leads to an increase in pressure on the advancing side and a decrease in pressure on the retreating side. Moreover, since the leading-edge radius is of the order of the size of the vortex core, the tip vortex bends around the leading edge of the pylon before being severed.[27] Due to the increased velocity on the retreating side, the vortex bends more over the retreating side.[15]

To obtain more information regarding the tip-vortex impingement process at the leading edge, Fig. 11 presents the axial velocity distribution in the tip-vortex impingement region at the leading edge of the pylon for three phase angles, obtained from the planar PIV setup. In this setup the clean pylon model was used, and thus the leading-edge radius of the airfoil was slightly smaller than for the microphone measurements. Again the velocity difference with respect to the propeller-off case is used to identify the effect of the tip vortex. In Fig. 11 the flow goes from left to right, and the top and bottom halves of the plots indicate retreating and advancing blade sides respectively, i.e. the top side is the “suction” side of the airfoil ($\alpha = 0°$). The plots can be interpreted as looking at the leading-edge plane represented in Fig. 4 from below.

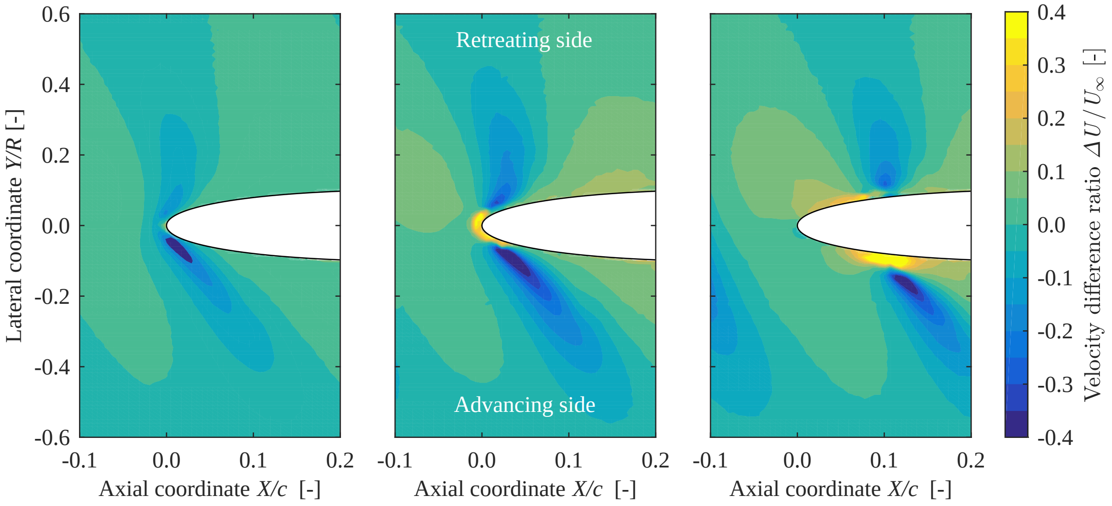

a) ϕ **= 92.5°** **b)** ϕ **= 97.5°** **c)** ϕ **= 120°**

Figure 11. Axial velocity distributions in the tip region ($r/R = 0.98$) for three different phase angles at $U_\infty = 40$ m/s.

The vortex impingement process shown in Fig. 11 is the cause of the large pressure fluctuations at the leading edge near $r/R = 1$ in Fig. 8. Figure 11a shows that at $\phi = 92.5°$ the tip vortex was nearly tangent to the plane, inducing velocities in negative X-direction. On the advancing side the vortex remained fairly undeformed, forming an oblique angle (the helix pitch angle) with the X-axis. Due to the angle of attack induced by the slipstream, on the retreating side the vortex was locally accelerated and bent around the leading edge. A small instant later, at $\phi = 97.5°$ (Fig. 11b), the vortex filament had wrapped around the leading edge. For this phase angle a segment of the vortex filament penetrated the plane, leading to an increase in axial velocity in the plane near the leading edge. This spanwise displacement of the vortex during the bending process was a consequence of an image-vortex effect,[15] which induced velocities in the positive Z-direction. Note that this local spanwise displacement during the bending process, which depends on parameters such as tip-vortex strength and leading-edge radius, is not related to the gradual spanwise displacement along the pylon chord observed in Fig. 8, which is a consequence of spanwise variations in lift along the pylon. Finally, at $\phi = 120°$ (Fig. 11c) the vortex filament had been cut in two, and the two segments were independently convected downstream along each side of the pylon. On the retreating side, the segment closest to the airfoil was almost parallel to the airfoil surface. The increased bending of the tip vortex on the retreating side during the impingement process leads to the differences between the two pylon sides shown in Fig. 10. At $\phi = 120°$ it can also be seen that on the advancing side the vortex penetrated the plane further than on the retreating side. This was due to the gradual spanwise displacement of the vortex as it was convected along the chord.

IV.C. Integral Unsteady Pylon Loading

The pressure distributions measured with the surface microphones were used to evaluate the structure-borne noise indicators defined by Eqs. 2 and 3. This allowed for a quantitative comparison of the pressure fluctuations ($\tilde{C}_{p,\text{mean}}$) and overall unsteady loading ($\tilde{C}_{L,\text{rms}}$) on the pylon for different operating conditions without considering the structural details of the pylon.

IV.C.1. Mean Pressure Fluctuations

The average amplitude of the pressure fluctuations on the pylon was evaluated for different values of advance ratio, propeller–pylon spacing, and angle of attack. Figure 12 presents $\tilde{C}_{p,\text{mean}}$ under these conditions.

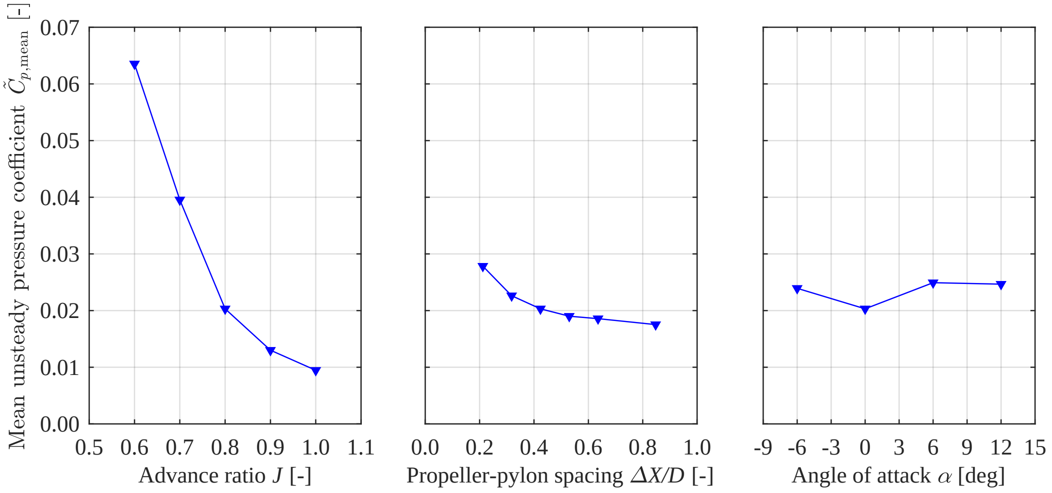

a) Effect of advance ratio ($\Delta X/D$ = 0.42, α = 0^0) **b) Effect of propeller-pylon spacing (J = 0.8, α = 0^0)** **c) Effect of angle of attack (J = 0.8, $\Delta X/D$ = 0.42)**

Figure 12. Average unsteady pressure coefficient versus advance ratio, propeller–pylon spacing, and angle of attack.

Figure 12a shows that $\tilde{C}_{p,\text{mean}}$ did not present a linear dependence on advance ratio. As the zero thrust setting is approached at $J = 1.0$ (see Fig. 6), the magnitude of the slope of the curve of Fig. 12a decreases and $\tilde{C}_{p,\text{mean}}$ approaches a positive finite value. This is because for an unloaded blade the tip-vortex strength tends to zero, while the blade wake remains. Nonetheless, Fig. 12a shows that the total amount of vibrational energy available for structure-borne noise decreased with advance ratio, dropping by 85% from $J = 0.6$ to $J = 1.0$. $\tilde{C}_{p,\text{mean}}$ also decreased with increasing propeller–pylon spacing, as visible in Fig. 12b. This agrees with the observations of Unruh,[5] and is attributed mainly to the viscous dissipation and diffusion of the tip vortex and blade wakes. Finally, Fig. 12c shows that the amplitude of the pressure fluctuations remained practically constant with angle of attack. $\tilde{C}_{p,\text{mean}}$ was slightly higher at $\alpha = \pm 6°$ than it was at zero angle of attack. It was found that at $\alpha = -6°$ this was due to an increase in fluctuations in the tip-vortex path on the retreating side of the pylon. At $\alpha = +6°$, on the other hand, the increase was a consequence of the pressure fluctuations at the flow reattachment location behind the separation bubble which appeared near the leading edge of the pylon. At $\alpha = 12°$, the average pressure fluctuations were again slightly lower since the retreating side of the pylon had stalled and hence the effect of the tip vortex on the retreating side was no longer appreciable.

IV.C.2. Unsteady Lift Coefficient

The integral unsteady pylon loading is compared for different advance ratios and propeller–pylon spacing values in Fig. 13 by means of the rms of the unsteady lift coefficient. The tendency of integrated unsteady pylon loading with angle of attack has not been included, since the convective velocity estimation did not provide reliable results at $\alpha = -6°$ and $\alpha = 12°$, and thus no conclusion can be drawn in this regard. The lift coefficient obtained from the original low-resolution pressure distribution has also been included in Fig. 13 for reference. The evident difference between the results based on interpolated and original pressure distributions in Fig. 13 confirms the importance of having a high spatial resolution.

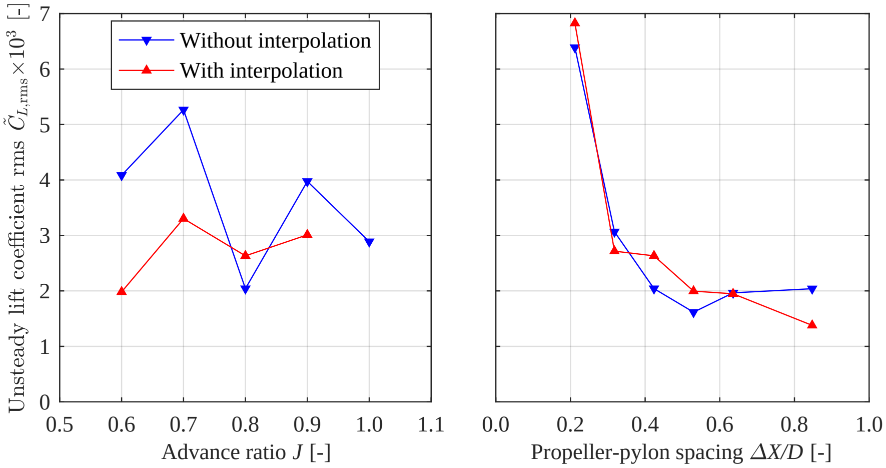

a) Effect of advance ratio
($\Delta X/D$ = 0.42, α = 0°)

b) Effect of propeller-pylon spacing
(J = 0.8, α = 0°)

Figure 13. Rms of the unsteady lift coefficient versus advance ratio and propeller–pylon spacing.

From Fig. 13 it can be seen that the amplitude of the unsteady lift coefficient was one to two orders of magnitude smaller than conventional lift coefficients on wings. This is in contrast with the recorded maximum unsteady pressure coefficients, which were of the same order of magnitude as typical steady-state pressure coefficients. The total unsteady pylon loading presented a non-monotonic behavior with advance ratio (Fig. 13a). This is because two factors play an important role in unsteady pylon loading: the amplitude of the pressure fluctuations and their distribution, i.e. the relative phase shifts of the excitations.

As visible in Fig. 12a, the amplitude of the pressure fluctuations decreased with increasing advance ratio. However, the advance ratio also has a direct effect on the pitch of the slipstream helix. The problem can be simplified by supposing that the pressure distribution on the pylon surface is sinusoidal in chordwise direction and constant in spanwise direction, as shown in Fig. 14. The simplification made in this reasoning is acceptable since the pylon and propeller blades presented no sweep, and moreover it was observed that the resulting unsteady lift coefficient was quasi-sinusoidal at all considered advance ratios.

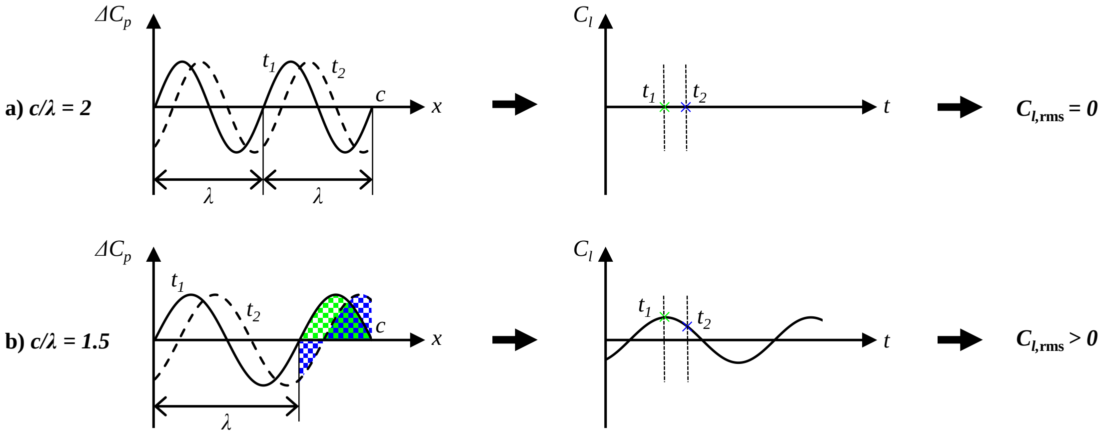

Figure 14. Graphical representation of an airfoil subjected to a sinusoidal pressure excitation (left) and consequent lift history (right) for two chord-to-wavelength ratios.

From Fig. 14 it becomes evident that in an ideal case, if the chord length of the pylon is an integer multiple of the wavelength of the excitation (λ), the resulting total unsteady loading is zero for each instant of time. It can therefore be concluded that the ratio between the slipstream pitch (i.e. the axial separation between consecutive tip vortices) and the pylon chord has a large influence on unsteady loading. This is supported by the results presented in Fig. 13b, which show that the integral unsteady pylon loading decreased with increasing propeller–pylon spacing. The advance ratio of the slipstream is, in first approximation, independent of propeller–pylon spacing, while the amplitude of the pressure fluctuations decreased with increasing spacing, as was shown in Fig. 12b. Therefore, the tendency of $\tilde{C}_{L,\mathrm{rms}}$ with propeller–pylon spacing is similar to the tendency of $\tilde{C}_{p,\mathrm{mean}}$. Below $\Delta X/D = 0.32$, Fig. 13 shows an exponentially large increase in $\tilde{C}_{L,\mathrm{rms}}$, which is approximately 2.5 times higher at $\Delta X/D = 0.21$ than at $\Delta X/D = 0.32$. This additional increase was attributed to two factors. Firstly, the static-pressure increase in the blade wakes was higher immediately behind the propeller disk, as visible in Fig. 7b. This increase in static pressure is known to have an exponential decay rate.[28] Secondly, the blade wakes were practically straight at $\Delta X/D = 0.21$ (see Fig. 7), and therefore impinged simultaneously along the pylon leading edge. By doubling the propeller–pylon spacing from the baseline $\Delta X/D = 0.42$ to $\Delta X/D = 0.84$, on the other hand, $\tilde{C}_{L,\mathrm{rms}}$ decreased by 48% . This percentage is however sensitive to parameters such as the operating conditions and geometry of the installation, and thus for a different configuration a comprehensive study will be required to analyze the combined effect of the different parameters.

V. Conclusions

The sources and magnitude of unsteady pylon loading occurring for a pylon-mounted tractor-propeller configuration have been studied using an experimental approach. Results from the experimental campaign show that for the baseline spacing of $\Delta X/D = 0.42$, the upstream effect of the pylon on the propeller is small, leading to an increase in thrust coefficient with respect to the isolated propeller of approximately 1%. This was comparable to the repeatability of the measurements.

Regarding the unsteady loading on the pylon, it is confirmed that the tip vortex is the dominant contributor to unsteady pylon loading, except when the blade is unloaded at low thrust settings, in which case the blade wakes become dominant. The pressure fluctuations created by the tip vortex are highest at the leading edge of the pylon, but persist along the chord as the tip vortex is convected downstream. In the blade-wake region, pressure fluctuations are appreciable only near the leading edge of the pylon. The average amplitude of the pressure fluctuations decreases with increasing advance ratio and propeller–pylon spacing, while it only presents minor variations with angle of attack. It is shown that the integral unsteady pylon loading, expressed using the rms of the unsteady lift coefficient, is not directly proportional to the strength of the blade wakes and tip vortices. The relative phase angles between the excitations on the pylon, which depend on advance ratio, have a large effect on unsteady loading. Increased propeller–pylon spacing, on the other hand, does decrease integral unsteady loading.

Based on the results of this study, it appears that the tip vortex path is the most effective region to apply surface treatments (e.g. porous material) in order to reduce unsteady loading, especially at the leading edge of the pylon. Furthermore, the quasi-sinusoidal unsteady lift coefficient confirms that strong reductions in structure-borne noise levels can be obtained if the structure is damped at the blade passage frequency. Finally, the data show that a pylon design tailored to the specific operating conditions of the propeller, for example by selecting a pylon chord length which is an integer multiple of the slipstream pitch, can have a significant effect on the aerodynamic excitation of the pylon and, therewith, on cabin noise levels.

References

[1] Magliozzi, B., Hanson, D. B., and Amiet, R. K., "Propeller and Propfan Noise," *NASA. Langley Research Center, Aeroacoustics of Flight Vehicles: Theory and Practice*, Vol. 1: Noise Sources, 1991, pp. 1–64.

[2] Block, P. J. W. and Gentry, G. L. J., "Directivity and Trends of Noise Generated by a Propeller in a Wake," NASA Technical Paper 2609, 1986.

[3] Goldsmith, I. M., "A study to define the research and technology requirements for advanced turbo/propfan transport aircraft," NASA Contractor Report 166138, 1981.

[4] Veldhuis, L. L. M., "Propeller Wing Aerodynamic Interference," PhD Dissertation, Delft University of Technology, 2005.

[5] Unruh, J. F., "Aircraft Propeller Induced Structure-Borne Noise," NASA Contractor Report 4255, 1989.

[6] Junger, M. C., Garrelick, J. M., Martinez, R., and Cole III, J. E., "Analytical model of the structureborne interior noise

induced by a propeller wake," NASA Contractor Report 172381, 1984.

[7] Martinez, R., "Predictions of Unsteady Wing and Pylon Forces Caused by Propeller Installation," NASA Contractor Report 178298, 1987.

[8] Miller, B. A., Dittmar, J. H., and Jeracki, R. J., "The Propeller Tip-Vortex – A Possible Contributor to Aircraft Cabin Noise," NASA Technical Memorandum 81768, 1981.

[9] Cole III, J. E., Westagard Stokes, A., Garrelick, J. M., and Martini, K. F., "Analytical Modeling of the Structureborne Noise Path on a Small Twin-Engine Aircraft," NASA Contractor Report 4136, 1988.

[10] Ljunggren, S., Samuelsson, I., and Widig, K., "Slipstream-Induced Pressure Fluctuations on a Wing Panel," *Journal of Aircraft*, Vol. 26, No. 10, 1989, pp. 914–919.

[11] Loeffler, I. J., "Structureborne Noise Control in Advanced Turboprop Aircraft," 25th AIAA Aerospace Sciences Meeting, Reno, NV, USA, 1987.

[12] Eversman, W., Koval, L. R., and Ramakrishnan, J. V., "A Comparison of the Structureborne and Airborne Paths for Propfan Interior Noise," NASA Contractor Report 180289, 1986.

[13] Vaicaitis, R. and Mixson, J. S., "Review of Research on Structureborne Noise," 26th Structures, Structural Dynamics, and Materials Conference, Orlando, FL, USA, 1985.

[14] SenGupta, G., Landmann, A. E., Mera, A., and Yantis, T. F., "Prediction of structure-borne noise, based on the finite element method," 10th AIAA Aeroacoustics Conference, Seattle, WA, USA, 1986.

[15] Thom, A. D., "Analysis of vortex-lifting surface interactions," PhD Dissertation, University of Glasgow, 2011.

[16] Swift, G. and Bartel, H. W., "Fluctuating Pressures on Wing Surfaces in the Slipstream of a Single-Rotor Propfan," 12th AIAA Aeroacoustics Conference, San Antonio, TX, 1989.

[17] Johnston, R. T. and Sullivan, J. P., "Unsteady Wing Surface Pressures in the Wake of a Propeller," *Journal of Aircraft*, Vol. 30, No. 5, 1993, pp. 664–651.

[18] Chiaramonte, J. Y., Favier, D., Maresca, C., and Agnes, A., "Unsteady Interactional Effects Between a Propeller and a Fixed Wing," 9th AIAA Applied Aerodynamics Conference, Baltimore, MD, 1991.

[19] Ragni, D., van Oudheusden, B. W., and Scarano, F., "3D pressure imaging of an aircraft propeller blade-tip flow by phase-locked stereoscopic PIV," *Experiments in fluids*, Vol. 52, 2012, pp. 463–477.

[20] Imaichi, K. and Ohmi, K., "Numerical processing of flow-visualization pictures – measurement of two-dimensional vortex flow," *Journal of Fluid Mechanics*, Vol. 129, 1983, pp. 283–311.

[21] Ragni, D., Ashok, A., van Oudheusden, B. W., and Scarano, F., "Surface pressure and aerodynamic loads determination of a transonic airfoil based on particle image velocimetry," *Measurement Science and Technology*, Vol. 20, 2009.

[22] van Oudheusden, B. W., "PIV-based pressure measurement," *Measurement Science and Technology*, Vol. 24, 2013.

[23] Della Corte, B., Sinnige, T., de Vries, R., Avallone, F., Ragni, D., Eitelberg, G., and Veldhuis, L. L. M., "Tractor Propeller–Pylon Interaction, Part II: Mitigation of Unsteady Pylon Loading by Application of Leading-Edge Porosity," 55th Aerospace Sciences Meeting, Grapevine, TX, 2017.

[24] Cremer, L., Heckl, M., and Petersson, B. A. T., *Structure-Borne Sound*, Springer, 3rd ed., 2005.

[25] Vér, I. L. and Beranek, L. L., *Noise and vibration control engineering: principles and applications*, John Wiley & Sons, 2006.

[26] Romano, G. P., "Analysis of two-point velocity measurements in near-wall flows," *Experiments in Fluids*, Vol. 20, 1995, pp. 68–83.

[27] Rockwell, D., "Vortex-body interactions," *Annual Review of Fluid Mechanics*, Vol. 30, 1998, pp. 199–299.

[28] Prato, J. and Lakshminarayana, B., "Investigation of Compressor Rotor Wake Structure at Peak Pressure Rise Coefficient and Effects of Loading," *Journal of Turbomachinery*, Vol. 115, No. 3, 1993, pp. 487–500.